FVC: A Novel Nonmagnetic Compass

Wenjun Lv, Yu Kang, *Senior Member, IEEE*, and Yun-Bo Zhao, *Senior Member, IEEE*

***Abstract*—The accurate orientation measurement in real time contributes significantly to the control of mobile robots, and further assists them to realize some fundamental functions, such as automatic pilot, cargo delivery, target tracking, etc. The traditional magnetic compass has been denounced for its susceptibility to ferro or electromagnetic materials, vehicular motion, and latitude variation. Hence, in this paper, we aim at proposing a novel nonmagnetic compass named floor visual compass (FVC) for mobile robots working in controlled indoor scenarios, which is mainly implemented by a downward-looking monocular camera. With previously laid auxiliary strips on the floor, which are parallel to the reference axis, the FVC is able to estimate the robot's orientation by means of image processing technologies and interval arithmetics. Considering the computational complexity of the visual orientation measurement, an event trigger for FVC is designed, to reduce the frequency of the correction operation using the visual orientation measurements. The real-world experiment verifies the effectiveness of the proposed nonmagnetic compass.**

***Index Terms*—Mobile robot, monocular vision, nonmagnetic compass, orientation measurement.**

I. Introduction

A COMPASS is a device used to determine the orientation angle relative to a given reference direction, which is of great importance to vehicular navigation, automatic pilot, disaster relief, and other domains related to automobile industry and advanced robotics [1]–[3]. For example, compasses play a crucial role in the reliability of the dead reckoning based localization, because a slight error occurring in the orientation measurement may give rise to a large error in localization over time [4]. Therefore, the investigations concerning compasses have attracted the attention from both academia and industry, to develop various compasses applicable to different scenarios.

As a usual compass, a magnetometer is capable of detecting the magnetism's components relative to different axes, thus providing the orientation with respect to geomagnetic north. Due to the susceptibility to magnetic interference, it is usually be used in combination with a gyroscope [5]. With the aid of a gyroscope, the measurements polluted by magnetic interference can be recognized and isolated, and finally, the reliability of the orientation estimation can be guaranteed by using a self-tuning fault-tolerant Kalman filter [6]. These magnetometer-involved orientation measurement approaches are usually used in the scenarios where geomagnetic field has no serious distortion. However, they may meet a mass of ferro and electromagnetic interference indoor, especially in the industrial environments. Additionally, a magnetometer also suffers from the uncertainties caused by robot motion (e.g., acceleration or deceleration), and becomes unstable near the geographic poles. Hence, the use of magnetic compasses should be avoided if possible in indoor scenarios [7].

Using positioning systems to estimate the robot's orientation can be read as a nonmagnetic compass, so that we named it positioning system based compass (PSC). With resorting to a two-antenna GPS receiver, the PSC is able to determine the robot's orientation by means of the double difference method [8]. For the mobile robots equipped with a portable GPS receiver, which has only one antenna, the robot's velocity components are first estimated by the difference-based approach or filter-based approach, and therefore, the orientation can be calculated directly via using the estimated velocities [9]. As compared with a magnetic compass, the PSC is not affected by the ferro or electromagnetic interference, and it performs better at the places near the polar regions. However, receiving the satellite signal may not be as reliable as needed in the building-dense areas, due to the possibly impossible establishment of the line-of-sight communication required between the receiver and the satellite [10], thus degrading the accuracy and reliability of the PSC.

These years have witnessed the development of the application of vision in the pose estimation of mobile robots. The off-board vision utilizes a camera mounted on the ceiling or wall to capture images containing the target mobile robot, and therefore, the computer is able to calculate its pose by measuring the robot profile or a specific marker on the robot's top [11], [12]. However, because an off-board camera is stationary, the limited field-of-sight has constrained the moving area of a mobile robot. Thus, it is not preferred in large-area applications. On the contrary, the onboard method uses a camera directly mounted on

Manuscript received February 23, 2018; revised June 8, 2018 and October 15, 2018; accepted November 11, 2018. Date of publication December 7, 2018; date of current version May 31, 2019. This work was supported in part by the National Natural Science Foundation of China under Grant 61725304, Grant 61673361, and Grant 61673350, in part by the Youth Top-Notch Talent Support Program, and in part by the Youth Yangtze River Scholar. *(Corresponding author: Yu Kang.)*

W. Lv is with the Department of Automation, University of Science and Technology of China, Hefei 230027, China (e-mail: wlv@ustc.edu.cn).

Y. Kang is with the State Key Laboratory of Fire Science, Department of Automation and Institute of Advanced Technology, University of Science and Technology of China, Hefei 230027, China, and also with the Key Laboratory of Technology in GeoSpatial Information Processing and Application System, Chinese Academy of Sciences, Beijing 100190, China (e-mail: kangduyu@ustc.edu.cn).

Y.-B. Zhao is with the College of Information Engineering, Zhejiang University of Technology, Hangzhou 310023, China (e-mail: ybzhao@ieee.org).

Color versions of one or more of the figures in this paper are available online at http://ieeexplore.ieee.org.

Digital Object Identifier 10.1109/TIE.2018.2884231

the mobile robot. For example, in [13] and [14], omnidirectional images are exploited to estimate the robot's pose by means of machine learning technologies and consolidated environmental features. With an Red-Green-Blue (RGB)-D camera and known two-dimensional blueprint, the pose in six degree-of-freedom can be estimated by using a particle filter [15]. Similar work can be seen in [16]–[18]. Although these methods adopting natural features can be used in uncontrolled environments, they are not practicable in industrial scenarios because of high computational complexity and feature mismatching issues. In controlled environments, it is preferred to employ artificial landmarks such as quick response (QR) codes. The QR coder, which contains the environmental information, is a frequently used landmark laid on the ceiling, wall, or floor [19]. However, the precise identification of QR coders requires a clearly captured image, which may not be satisfied if the robot is in high speed, or the camera has low maximum frame rate.

According to the aforementioned reasons, we aim at a novel nonmagnetic compass named floor visual compass (FVC) for mobile robots. The FVC is essentially an orientation determination system mainly composed of the auxiliary strips laid on the floor and a downward-looking camera. In the FVC setting, the auxiliary strips parallel to the reference axis are first laid on the floor of the working area. These auxiliary strips has the complementary color in hue compared with the floorings, and the same spacings. The relative angle between the mobile robot and the auxiliary strips can then be extracted from the floor images. However, since the quadrant in which the robot's orientation lies is unknown, only one of two possible values in the visual orientation measurement is the real one. Hence, we further propose an estimation algorithm to identify the real measurement and calculate the robot's orientation by means of interval arithmetics. Finally, considering the computational complexity of the visual orientation measurement, an event trigger for the FVC is designed to reduce the frequency of the correction operation using the visual orientation measurements.

The proposed FVC has the following merits compared with existing methods. First, the FVC is nonmagnetic, making it suitable for many industrial applications where the ferro or electromagnetic interference may fail the frequently used magnetic compasses. Second, the FVC adapts to high-speed robots, while the nonmagnetic compass such as the QR coder based compass, QRC, fails because of the motion blur induced problem. Additionally, the FVC barely suffers from the blocked line-of-sight problem because the camera lens is close to the floor, and the FVC does not cause privacy issues since the camera will not capture images of human bodies or faces. Finally, the FVC may use natural auxiliary strips such as tile joints to function, making it applicable to many scenarios where no changes of environment can be made and thus fails QRC.

The rest of the paper is organized as follows. Section II covers some necessary preparatory work before the use of FVC, including the auxiliary strips layout and perspective transformation experiment. Section III presents the approach to acquire the visual orientation measurement by using the captured floor images. Section IV expatiates the orientation estimation method by means of interval arithmetics. Section V gives the experimental evaluation based on a real-world differential-drive mobile robot. The paper is concluded in Section VI.

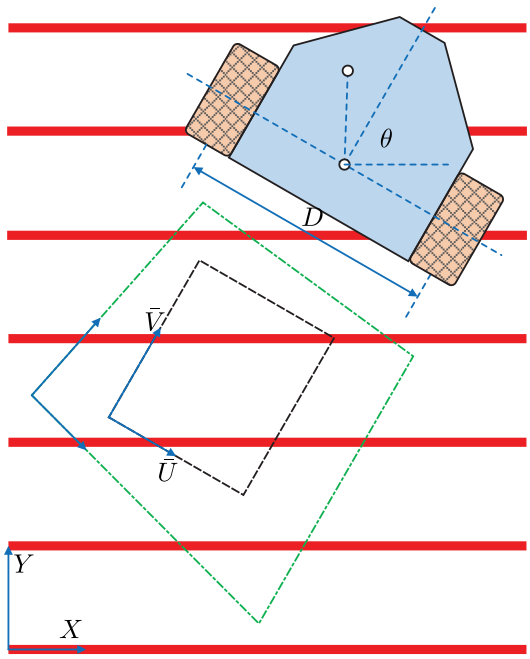

Fig. 1. Illustration of the FVC from top view. The meshed yellow rectangles represent the robot's wheels and the blue polygon its body. The floor is covered with red auxiliary strips, which are all parallel to the X-axis. Any two adjacent strips have the equal spacing. The green dashed quadrilateral is the floor area that the downward-looking camera could capture.

II. Preparatory Work

In this section, we present some necessary preparations before the use of FVC, including the layout of auxiliary strips and the acquirement of perspective transformation function.

The robot's orientation θ is defined as the counterclockwise rotational angle from X-axis to the robot's forward direction. If the downward-looking camera can capture the X-axis, the angle of robot's forward direction with respect to the X-axis can be calculated, and furthermore, θ can be obtained. In reality, the camera cannot capture the X-axis when the mobile robot is not close to it. For this reason, we should lay some auxiliary strips on the floor, which can be read as the copies of the X-axis. As seen in Fig. 1, the floor is covered with red auxiliary strips, which are all parallel to the X-axis. The intervals between any two adjacent auxiliary strips are the same. The colors of the auxiliary strips are optional, but they should be complementary to the flooring's colors in hue, or in brightness.[1]

The FVC can function provided the downward-looking camera can capture at least one auxiliary strip at any location. To satisfy this premise, one can enlarge the camera's view field, by decreasing the strips' interval, increasing the camera's height, or adjusting the camera's posture. Consider the situation where the camera's height and posture are fixed. One can adjust the strips'

[1]For example, the auxiliary strips are in yellow (or black), while the flooring is in blue (or white).

interval from wide to narrow, until the camera can capture at least one auxiliary strip, thereby obtaining the *maximum strip's interval*. On the other hand, the allowed strip's interval may be as small as possible, as long as each strip can be identified from the image. Because each strip provides the same information related to the robot's orientation, extra strips captured by the camera rarely affect the accuracy of orientation estimation.

As illustrated in Fig. 1, the camera's field-of-sight is represented by green dashed quadrilateral. Via adjusting the camera's posture, an inner rectangle of the field-of-sight can be found, the shorter edge of which is longer than the strip's interval. Mapping the four rectangular corners with respect to the U–V coordinate system into those with respect to the $\bar{U}$–$\bar{V}$ coordinate system, the perspective transformation function

$$(\bar{u}, \bar{v}) = \mathfrak{P}\{(u, v)\} \tag{1}$$

can be achieved. The X–Y coordinate system is same as the $\bar{U}$–$\bar{V}$ coordinate system in scale.

III. Visual Orientation Measurement

In this section, we present the orientation measurement by using the monocular vision, which is elementary yet crucial to the success of FVC. The central lines of the auxiliary strips are first extracted and parameterized. Second, by using the perspective transformation function, the parameters of the central lines with respect to $\bar{U}$–$\bar{V}$ coordinate system are obtained. After converting these parameters into the robot's orientation, the visual orientation measurement can be realized finally.

A. Image Preprocessing

We exploit some fundamental image processing technologies, such as thresholding segmentation, mathematical morphology, perspective transform, and Hough transformation, to extract the central lines of the auxiliary strips. Because these technologies are mature, we only present the outline of the preprocessing procedure, rather than a detailed description.

1) Auxiliary Strips Extraction: The original image $\mathbb{O}_t$ captured at sampling point t is relative to the RGB colors space. In order to facilitate the extraction of the auxiliary strips from the floorings, $\mathbb{O}_t$ is first transformed into a colored image $\mathbb{I}_t$ with respect to the Hue-Saturation-Brightness (HSB) colors space. Consequently, applying HSB-based thresholding segmentation to $\mathbb{I}_t$, a binary image $\mathbb{B}_t$ is obtained, which is expected to contain the auxiliary strips only. If the robot's working environment is not of enough illumination, the threshold of saturation and brightness is set as a lower value to guarantee the segmentation of the auxiliary strips.

2) Central Lines Extraction: One auxiliary strip is expected to be represented by a set of parameters, so its central lines are extracted. First, due to the uneven colors distribution, the hole-filling operation is conducted on $\mathbb{B}_t$, which avoids too many connected components existing in the floor image. Second, the skeletons of the auxiliary strips, which is read as the central lines, can be obtained by iterative morphological erosion operations. After skeletonization, some parasitic components are inevitably preserved because of the non smoothness of the extracted auxiliary strips. For the parasitic components disconnected to the central lines, the lengths of which are much smaller, we can prune them by removing the connected components whose pixel amounts are smaller than a certain value. For the parasitic components connected to the central lines, which are frequently referred to as spurs, they can be pruned by iteratively removing one terminal pixel. After conducting these operations successively on $\mathbb{B}_t$, we finally obtain a binary image $\widehat{\mathbb{B}}_t$ containing the central lines of the auxiliary strips only.

B. Line Detection

Now we are in the position to detect the central lines in $\widehat{\mathbb{B}}_t$ by applying Hough transformation. First, the lines are parameterized by

$$u\cos\rho + v\sin\rho = r \tag{2}$$

where $r \in [r_{\min}, r_{\max}]$ denotes the perpendicular distance from the origin of the U–V coordinate system to the line and $\rho \in [-\frac{\pi}{2}, \frac{\pi}{2})$ denotes the angle from the U-axis to the perpendicular. Hence, each line can be mapped to the (r, ρ)-space (also known as the Hough space) as a point. Second, the Hough space is quantized such that it yields an $N_\rho \times N_r$ matrix A, which is referred to as an accumulator matrix. It is noted that the determination of N_ρ and N_r meets a tradeoff between accuracy and computational complexity. If the Hough space is quantized in higher resolution, namely, larger N_ρ and N_r, the detection of ρ can be more accurate, and therefore, the visual orientation measurement is higher in accuracy. However, quantized Hough space in higher resolution means more time-consuming. If the algorithm is realized on a high-performance digital device, then the computational time can be extremely small, and therefore N_ρ and N_r can be set as larger integers.

For a $\mu \times \nu$ image, we have

$$r_{\max} = -r_{\min} = \sqrt{\mu^2 + \nu^2} \tag{3}$$

and the accumulator matrix A has N_ρ elements equally dividing the interval $\rho \in \left[-\frac{\pi}{2}, \frac{\pi}{2}\right)$ and N_r elements equally dividing the interval $r \in [r_{\min}, r_{\max}]$. The matrix indices are integers $(i, j) \in \mathbb{Z}^2$ that

$$i \in [1, N_\rho] \mapsto \rho \in \left[-\frac{\pi}{2}, \frac{\pi}{2}\right) \tag{4a}$$

$$j \in [1, N_r] \mapsto r \in [r_{\min}, r_{\max}]. \tag{4b}$$

Furthermore, each pixel point (u, v) votes for all the lines existing within the quantized Hough space, and furthermore, the potential lines represented by (r, ρ)-pairs can be determined by calculating the peak values of the elements in the accumulator matrix. For every line, two or more (r, ρ)-pairs with small differences may be obtained because of the imperfection of the pruning algorithm. To solve this problem, the (r, ρ)-pairs are clustered using the k-means method. That is, two different pairs, (r_i, ρ_i)-pair and (r_j, ρ_j)-pair, $i \neq j$, belong to one cluster if and only if the following conditions hold:

$$|r_i - r_j| \leq \sigma_r \tag{5a}$$

$$|\rho_i - \rho_j| \leq \sigma_\rho \tag{5b}$$

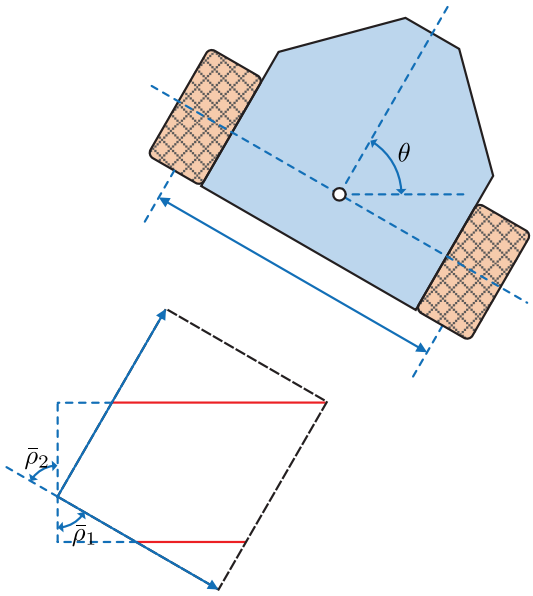

Fig. 2. Illustration of the relationship of $\bar{\rho}$ and θ in Case 1.

where σ_r and σ_ρ are the similarity thresholds determined empirically. The average of (r, ρ)-pairs clustered in one group can serve as the final outputs of the line detection.

Finally, the (r, ρ)-pairs with respect to the U–V coordinate system are converted to $(\bar{r}, \bar{\rho})$-pairs with respect to the $\bar{U}$–$\bar{V}$ coordinate system. Find two points on the (r, ρ)-line, the coordinates of which are (u_1, v_1) and (u_2, v_2), and then calculate

$$(\bar{u}_1, \bar{v}_1) = \mathfrak{P}\{(u_1, v_1)\} \tag{6a}$$

$$(\bar{u}_2, \bar{v}_2) = \mathfrak{P}\{(u_2, v_2)\} \tag{6b}$$

where $(\bar{u}_1, \bar{v}_1)$ and $(\bar{u}_2, \bar{v}_2)$ are two points on the lines with respect to the $\bar{U}$–$\bar{V}$ coordinate system. Substituting them to (2), we have

$$\bar{u}_1 \cos\bar{\rho} + \bar{v}_1 \sin\bar{\rho} = \bar{r} \tag{7a}$$

$$\bar{u}_2 \cos\bar{\rho} + \bar{v}_2 \sin\bar{\rho} = \bar{r} \tag{7b}$$

and therefore, we obtain that

$$\bar{\rho} = \begin{cases} \arctan\dfrac{\bar{u}_1 - \bar{u}_2}{\bar{v}_2 - \bar{v}_1}, & \text{when } \bar{v}_1 \neq \bar{v}_2 \\ -\dfrac{\pi}{2}, & \text{when } \bar{v}_1 = \bar{v}_2 \end{cases} \tag{8}$$

which realizes parameters transformation from the U–V coordinate system to the $\bar{U}$–$\bar{V}$ coordinate system.

C. Orientation Acquirement

In the previous step, the parameters of the auxiliary strips in the floor image are obtained, thereby yielding a certain number of $(\bar{r}, \bar{\rho})$-pairs. Now, we will determine the transformation rules from $\bar{\rho}$ to θ. The four cases where the robot's orientation θ lies in $(0, \frac{\pi}{2}]$, $(\frac{\pi}{2}, \pi]$, $(\pi, \frac{3\pi}{2}]$, and $(\frac{3\pi}{2}, 2\pi]$ are analyzed respectively.

Consider Case 1 that the value of robot's orientation lies in the first quadrant. As shown in Fig. 2, there are two parallel strips parameterized by $(\bar{r}_1, \bar{\rho}_1)$ and $(\bar{r}_2, \bar{\rho}_2)$. Because they are parallel to each other, all the auxiliary strips have the same angle, and therefore, the subscripts of $\bar{\rho}$ are ignored. Furthermore, we can easily obtain

$$\theta_{(\mathrm{c}1)} = -\bar{\rho} \tag{9}$$

where $\theta_{(\mathrm{c}1)} \in \left(0, \frac{\pi}{2}\right]$ denotes the value of robot's orientation in Case 1.

For Cases 2 to 4, via the similar analysis, we have

$$\theta_{(\mathrm{c}2)} = -\bar{\rho} + \pi \tag{10a}$$

$$\theta_{(\mathrm{c}3)} = -\bar{\rho} + \pi \tag{10b}$$

$$\theta_{(\mathrm{c}4)} = -\bar{\rho} \tag{10c}$$

where $\theta_{(\mathrm{c}2)} \in \left(\frac{\pi}{2}, \pi\right]$, $\theta_{(\mathrm{c}3)} \in \left(\pi, \frac{3\pi}{2}\right]$, and $\theta_{(\mathrm{c}4)} \in \left(\frac{3\pi}{2}, 2\pi\right]$ denote the robot's orientation in Case 2, Case 3, and Case 4, respectively. Combining (9), (10a), (10b), and (10c) yields

$$\theta \in \left\{\theta_{(\mathrm{c}1)}, \theta_{(\mathrm{c}2)}, \theta_{(\mathrm{c}3)}, \theta_{(\mathrm{c}4)}\right\} = \{-\bar{\rho}, -\bar{\rho} + \pi\} \tag{11}$$

and furthermore, considering $\theta \in [0, 2\pi)$, (11) is modified into

$$\theta \in \begin{cases} \{-\bar{\rho}, -\bar{\rho} + \pi\}, & \text{if } \bar{\rho} \in \left[-\frac{\pi}{2}, 0\right) \\ \{2\pi - \bar{\rho}, -\bar{\rho} + \pi\}, & \text{if } \bar{\rho} \in \left[0, \frac{\pi}{2}\right) \end{cases} \tag{12}$$

which reveals the transformation rules from $\bar{\rho}$ to θ.

Define $\bar{\rho}_t$ as $\bar{\rho}$ at sampling point t, and $\bar{\rho}_{c,t}$ the measurement of $\bar{\rho}_t$. Supposing

$$\bar{\rho}_{c,t} = \bar{\rho}_t + n_{c,t} \tag{13}$$

where $n_{c,t}$ denotes the measurement noise, which may be caused by the roundoff of Hough transformation and spurs connected to the strip's skeleton. It is assumed that $n_{c,t} \in [-R, +R]$ is an unknown-but-bounded noise where $R > 0$ denotes the bound's radius.

Finally, the visual orientation measurement $\Theta_{c,t}$ is obtained, that is

$$\Theta_{c,t} = \begin{cases} \{-\bar{\rho}_{c,t}, -\bar{\rho}_{c,t} + \pi\}, & \text{if } \bar{\rho}_{c,t} \in \left[-\frac{\pi}{2}, 0\right) \\ \{2\pi - \bar{\rho}_{c,t}, -\bar{\rho}_{c,t} + \pi\}, & \text{if } \bar{\rho}_{c,t} \in \left[0, \frac{\pi}{2}\right) \end{cases} \tag{14}$$

which is calculated by using the detected $\bar{\rho}_{c,t}$. Its relationship with θ_t can be described as

$$\Theta_{c,t} = \begin{cases} \{\theta_t + n_{c,t}, \theta_t + \pi + n_{c,t}\}, & \text{if } \theta_t \in [0, \pi) \\ \{\theta_t + n_{c,t}, \theta_t - \pi + n_{c,t}\}, & \text{if } \theta_t \in [\pi, 2\pi) \end{cases} \tag{15}$$

which will be used as an observation model to realize the orientation estimation algorithm in the following section. Obviously, as shown in (15), $\Theta_{c,t}$ contains a real measurement $\theta_{c,t}^{(\dagger)}$ equaling $\theta_t + n_{c,t}$, and a pseudo measurement $\theta_{c,t}^{(\sharp)}$ equaling $\theta_t + \pi + n_{c,t}$ or $\theta_t - \pi + n_{c,t}$, which gives rise to the difficulties in the orientation estimation.

IV. Orientation Estimation

This section expatiates how to estimate the robot's orientation only by using the visual orientation measurement. Generally speaking, the orientation estimation requires the information both from proprioceptive and exteroceptive sensors, to establish a system model and observation model, after which this problem

can be solved by using Kalman filter. However, without resorting to a proprioceptive sensor, the inner kinestates can also be measured by analysis of the actuator saturations.

Take a differential-drive mobile robot as an example. Due to the motors' saturations, the maximal rotational speeds of the left and right wheels (w_ℓ and w_r) can be readily obtained, that is, $\bar{w}_\ell$ and $\bar{w}_r$. Therefore, we have $w_{\ell,t} \in \mathcal{W}_\ell = [-\bar{w}_\ell, +\bar{w}_\ell]$ and $w_{r,t} \in \mathcal{W}_r = [-\bar{w}_r, +\bar{w}_r]$, followed by

$$\mathcal{W} = \frac{\mathcal{W}_\ell - \mathcal{W}_r}{D} \tag{16}$$

where $\mathcal{W} = [-\frac{\bar{w}_\ell + \bar{w}_r}{D}, +\frac{\bar{w}_\ell + \bar{w}_r}{D}]$ denotes the interval in which the robot's heading rate lies, and D denotes the robot's axle width.

Hence, the problem is to design an orientation estimation algorithm based on

$$\theta_t = \theta_{t-1} + T\delta_{t-1} \tag{17a}$$

$$\delta_t \in \mathcal{W} \tag{17b}$$

$$\Theta_{c,t} = \left\{\theta_{c,t}^{(\dagger)}, \theta_{c,t}^{(\sharp)}\right\} \tag{17c}$$

where θ_t denotes the robot's orientation, T the sampling interval, δ_t the heading rate, $\Theta_{c,t}$ the visual orientation measurement, $\theta_{c,t}^{(\dagger)}$ the real measurement, and $\theta_{c,t}^{(\sharp)}$ the pseudo measurement. Observe that (17a) and (17c) can be read as a system model and observation model, respectively. In most solutions, δ_t is seen as an input of the system model, which can be measured by proprioceptive sensors, like a gyroscope or odometry. However, if we only have the knowledge of the upper and lower bounds of δ_t, rather than an accurate measurement, δ_t is read as the system noise.

Because the probability distribution of δ_t is unknown, we dispose this problem by means of interval arithmetics. In the following, we use the notation $\mathcal{I} = [a, b] = \{x \in \mathbb{R} : a \le x \le b\}$ to denote an interval with lower bound a, and upper bound b, $\mathrm{mid}(\mathcal{I}) = \frac{a+b}{2}$ the interval's midpoint, $\mathrm{rad}(\mathcal{I}) = \frac{b-a}{2}$ the interval's radius, $\mathrm{wid}(\mathcal{I}) = b - a$ the interval's width, $\max(\mathcal{I}) = b$ and $\min(\mathcal{I}) = a$ the upper bound and lower bound, respectively. For two intervals $\mathcal{I}_1 = [a_1, b_1]$ and $\mathcal{I}_2 = [a_2, b_2]$, their addition operation and intersection operation are defined as

$$\mathcal{I}_1 + \mathcal{I}_2 = [a_1 + a_2, b_1 + b_2] \tag{18a}$$

$$\mathcal{I}_1 \cap \mathcal{I}_2 = [\max(a_1, a_2), \min(b_1, b_2)] \tag{18b}$$

respectively. If $\min(\mathcal{I}_1 \cap \mathcal{I}_2) > \max(\mathcal{I}_1 \cap \mathcal{I}_2)$, then $\mathcal{I}_1 \cap \mathcal{I}_2 = \emptyset$. More definitions and formulae can be seen in [20]. Additionally, in the following, the notation $\widehat{\mathcal{I}}_t$ denotes the corrected estimation interval, $\widetilde{\mathcal{I}}_t$ the predicted estimation interval, $\mathcal{I}_{\delta,t} = \mathcal{W}$ the robot's heading interval, and $\mathcal{I}_{c,t}^{(\dagger)} = [\theta_{c,t}^{(\dagger)} - R, \theta_{c,t}^{(\dagger)} + R]$ and $\mathcal{I}_{c,t}^{(\sharp)} = [\theta_{c,t}^{(\sharp)} - R, \theta_{c,t}^{(\sharp)} + R]$ denote the real measurement interval and pseudo measurement interval.

A. Estimation Algorithm

1) Initialization: The initial corrected estimation interval $\widehat{\mathcal{I}}_0 = \mathcal{I}(\hat{\theta}_0, \widehat{P}_0)$ is determined artificially, where $\mathrm{rad}(\widehat{\mathcal{I}}_0) \le R$.

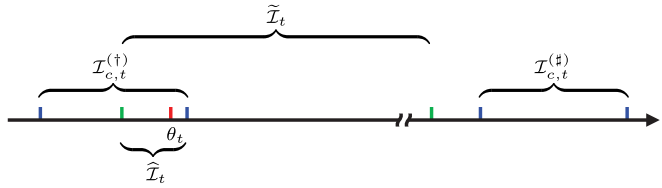

Fig. 3. Graphic representations of true value of robot's orientation δ_t, the predicted estimation interval $\widetilde{\mathcal{I}}_t$, the corrected estimation interval $\widehat{\mathcal{I}}_t$, the visual orientation measurement intervals $\mathcal{I}_{c,t}^{(\dagger)}$, and $\mathcal{I}_{c,t}^{(\sharp)}$.

2) Predicted Estimation: Suppose that $\widehat{\mathcal{I}}_{t-1}$ has been obtained, then the predicted estimation interval $\widetilde{\mathcal{I}}_t$ can be achieved by

$$\widetilde{\mathcal{I}}_t = \widehat{\mathcal{I}}_{t-1} + \mathcal{I}_{\delta,t-1}. \tag{19}$$

3) Corrected Estimation: The corrected estimation interval $\widehat{\mathcal{I}}_t$ can be readily achieved by

$$\widehat{\mathcal{I}}_t = \bigcup_{i=1}^{2} \left(\widetilde{\mathcal{I}}_t \cap \mathcal{I}_{c,t}^{(i)}\right) \tag{20}$$

where $\mathcal{I}_{c,t}^{(i)}$ denotes the measurement interval generated by the ith element in $\Theta_{c,t}$. The midpoint $\mathrm{mid}(\widehat{\mathcal{I}}_t)$ can be regarded as a point estimation, yet not the optimal estimation, for the absence of the knowledge of system noise's probability distribution.

B. Pseudo Measurement Isolation

In (20), to ensure $\widehat{\mathcal{I}}_t$ is an interval, it should be guaranteed that only one of $\mathcal{I}_{c,t}^{(1)}$ and $\mathcal{I}_{c,t}^{(2)}$ intersects with $\widetilde{\mathcal{I}}_t$. In other words, the pseudo measurement $\theta_{c,t}^{(\sharp)}$ should be isolated. Now we give the requirement that the pseudo measurement can be isolated.

Because $|\theta_{c,t}^{(\dagger)} - \theta_{c,t}^{(\sharp)}| = \pi$, we first consider the case where $\theta_{c,t}^{(\sharp)} = \theta_{c,t}^{(\dagger)} + \pi$. As shown in Fig. 3, it should be guaranteed that

$$\max(\widetilde{\mathcal{I}}_t) < \min(\mathcal{I}_{c,t}^{(\sharp)}) \tag{21}$$

or

$$\begin{aligned}\mathrm{wid}(\widetilde{\mathcal{I}}_t) &= \max(\widetilde{\mathcal{I}}_t) - \min(\widetilde{\mathcal{I}}_t) \\ &< \min(\mathcal{I}_{c,t}^{(\sharp)}) - \min(\widetilde{\mathcal{I}}_t)\end{aligned} \tag{22}$$

under the condition that

$$\min(\widetilde{\mathcal{I}}_t) \le \delta_t \le \max(\mathcal{I}_{c,t}^{(\dagger)}). \tag{23}$$

Hence, the requirement that the pseudo measurement can be isolated is obtained as

$$\begin{aligned}\mathrm{wid}(\widetilde{\mathcal{I}}_t) &< \inf\{\min(\mathcal{I}_{c,t}^{(\sharp)}) - \min(\widetilde{\mathcal{I}}_t)\} \\ &= \min(\mathcal{I}_{c,t}^{(\sharp)}) - \max(\mathcal{I}_{c,t}^{(\dagger)}) \\ &= \pi - 2R.\end{aligned} \tag{24}$$

The same requirement can be obtained for the other case $\theta_{c,t}^{(\sharp)} = \theta_{c,t}^{(\dagger)} - \pi$ by the analogous analysis.

C. Event-Triggering Mode

Because the visual orientation measurement is computationally complex, and there is no need to correct the predicted estimation at each sampling point, an event trigger is designed to enable the corrected estimation based on the visual orientation measurement, according to the following two rules. First, the requirement shown in (24) should be always guaranteed, otherwise the corrected estimation interval will not be consecutive. Second, all the widths of the corrected estimation intervals should be lower than ϖ, a non negative real number, which is determined by the users, thus preventing the uncertainties from getting too large. The event trigger $\lambda_t = \{0, 1\}$ is

$$\lambda_t = \begin{cases} 0, & \text{if } \mathrm{wid}(\widetilde{\mathcal{I}}_t + \widetilde{\mathcal{I}}_{\delta,t}) < \pi - 2R \text{ and } \mathrm{wid}(\widetilde{\mathcal{I}}_t) < \varpi \\ 1, & \text{otherwise} \end{cases} \tag{25}$$

where $\varpi \geq 0$ denotes the tolerable width. If ϖ is a small number approaching 0, the condition $\mathrm{wid}(\widetilde{\mathcal{I}}_t) < \varpi$ may never be satisfied, and therefore, $\lambda_t = 1$ at all sampling points.

Based on the event trigger λ_t, the estimation algorithm can work in event-triggering mode, by modifying (20) into

$$\widehat{\mathcal{I}}_t = \lambda_t \bigcup_{i=1}^{2} \left(\widetilde{\mathcal{I}}_t \cap \mathcal{I}_{c,t}^{(i)} \right) + (1 - \lambda_t) \widetilde{\mathcal{I}}_t. \tag{26}$$

D. Gyroscope Aided Version: GyroFVC

In Sections IV-A and IV-C, we describe how to estimate the orientation of the robot without resorting to the proprioceptive sensors (e.g., a gyroscope), where the orientation variation is measured by analyzing the actuator saturations. Such a duty may also be conducted by introducing a gyroscope, which can give rise to a more accurate measurement of the orientation variation than the nonsensor approach. This gyroscope assisted version of FVC, referred to as GyroFVC, can be derived straightforwardly from extending the standard FVC.

In fact, let ω_t be the gyroscopic reading at sampling point t, and Δ be the error radius of the unknown but bounded gyroscopic noise, and then the same orientation estimation algorithm can be used to GyroFVC directly after rewriting (17b) as $\delta_t \in \mathcal{I}_{\delta,t} = \mathcal{I}(\omega_t, \Delta)$.

V. Experimental Evaluation

In this section, we evaluate the proposed FVC by conducting real-world experiments on a differential-drive mobile robot, which has been equipped with a downward-looking camera, a consumer-grade gyroscope, an industrial-grade gyroscope and a magnetometer.

A. Experiment Setup

The photograph of the experimental robot and its configuration block diagram are shown in Fig. 4. The gray floor is covered with red strips parallel to the X-axis. All auxiliary strips have the same spacing distance of 500 mm. The experimental robot (Turtlebot3 Burger) is equipped with a consumer-grade gyroscope (MPU6500), an industrial-grade gyroscope (ADXRS453), a magnetometer (AK8963), and a downward-looking camera (manufactured by RMONCAM). The specifications of these devices are listed in Table I. It is worth pointing out that the camera used in the experiment is of relatively low performance specifications, and the FVC can be implemented using any other camera with similar or higher performance specifications than the one used here. The first gyroscope is used to aid the FVC to estimate the orientation of the robot, and the second gyroscope with a higher accuracy is used for reference purpose. Both gyroscopes are pre-calibrated using the algorithm proposed in [21]. The magnetometer, which detects the magnetic intensity along each axis, serves as a magnetic compass. The camera has no distortion, thus not being calibrated. All these sensors are sampled every 0.1 s, and their readings are transferred to a computer (3.2 GHz with 8 GB RAM) via WiFi network. The computer also serves as a controller, which sends motion commands to the robot. After all data being collected, they can be processed by using MATLAB.

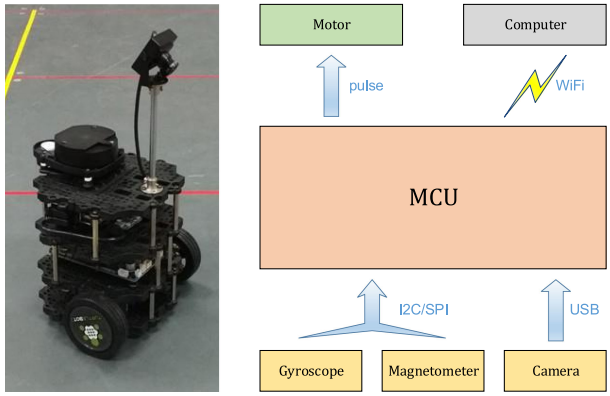

Fig. 4. Photograph of the experimental robot and its configuration block diagram.

TABLE I
SPECIFICATIONS OF THE SENSORS

Sensor	Specification
1st Gyroscope	range: ±250 deg/s; accuracy: ±5 deg/s.
2nd Gyroscope	range: ±400 deg/s; accuracy: ±0.4 deg/s.
Magnetometer	range: ±4800 uT.
Camera	normal lens; resolution: 480×640; rate: 30 fps.

B. Results and Analysis

1) Features Extraction of Auxiliary Strips: We select two typical images that contain environmental interference to exhibit the effectiveness of the central line detection of the auxiliary strips. As shown in Figs. 5 and 6, we use four images to show the procedure that the original image is processed, respectively. Obviously, the situation in Fig. 5 is brighter than that in Fig. 6. Hence, some sections of the auxiliary strips becomes white because of the reflection rendered by strong illumination, and therefore, the extracted auxiliary strips in the binary image are incomplete at some sections after the thresholding segmen-

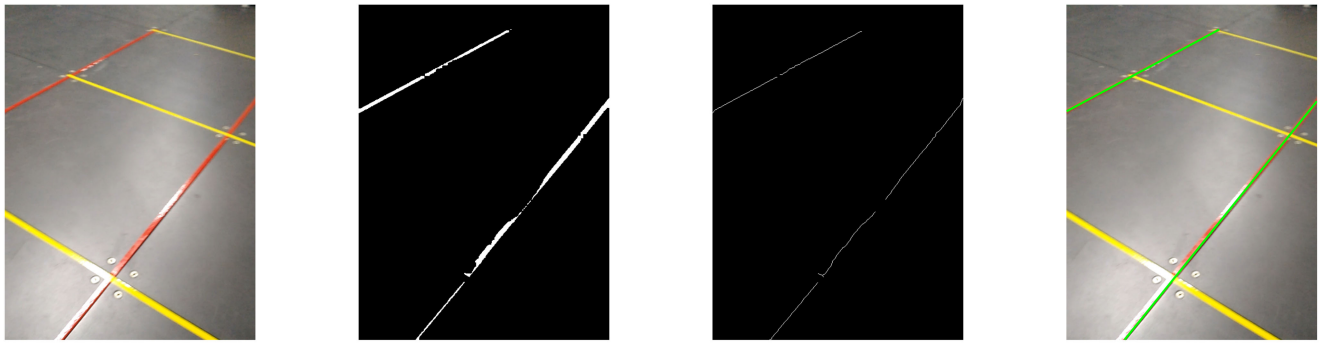

(a) (b) (c) (d)

Fig. 5. Test of the line detection of red auxiliary strips, under the interference of strong illumination. (a) Original image. (b) Segmentation and gaps filling. (c) Skeletonization and pruning. (d) Detected lines.

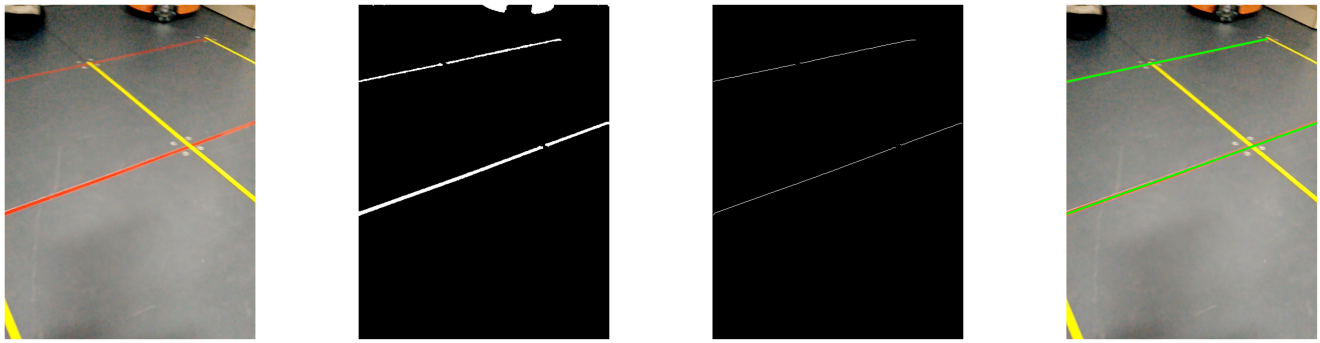

(a) (b) (c) (d)

Fig. 6. Test of the line detection of red auxiliary strips, under the interference of other objects. (a) Original image. (b) Segmentation and gaps filling. (c) Skeletonization and pruning. (d) Detected lines.

tation and gap filling operations. Additionally, this incompleteness has distinctly affected the extraction of the central lines, so the extracted lines are slightly waved after skeletonization and pruning. Finally, as the green lines show, the results slightly diverge to the central lines of the auxiliary strips, but not going out of the strip's range. These errors rendered by strong illumination are innocuous, and can be reduced by using materials with rough surfaces to implement the layout of auxiliary strips.

On the opposite way, the situation in Fig. 6 does not suffer from strong illumination, but the interference of some other environmental objects. In order to enlarge the camera's field-of-sight, its posture has been adjusted to be unparalleled to the floor, which results in that the camera may capture some objects undesired to be included, such as cabinets, shoes, or the legs of tables. In this situation, parts of an omnidirectional mobile robot appear in the original image, which has the similar colors with the red auxiliary strips. As a result, these parts are preserved after image binarization, because the thresholding segmentation cannot distinguish the difference with the auxiliary strips. Owing to that their skeletons have much fewer pixels than those of the auxiliary strips, the omnidirectional mobile robot is removed by applying the pruning algorithm. At last, the central lines are extracted perfectly. Although the detection of the central lines is not affected by these environmental interference, it is still needed to avoid the appearance of the objects whose colors is close to that of the auxiliary strips, in the field-of-sight of the camera.

2) Experiment of FVC: The estimation algorithm is initialized by $\widehat{\mathcal{I}}_0 = [27, 33]$ deg and $R = 6$ deg. Based on different event triggers, three tests are designed as follows.

1) *Test 1:* Using the visual orientation measurement to correct the predicted estimation at each sampling point.
2) *Test 2:* The FVC is in the event-triggering mode by using (25) where $\varpi = 60$ deg.
3) *Test 3:* The FVC is in the event-triggering mode by using (25) where $\varpi = \infty$.

In Test 1, $\lambda_t = 1$ at all sampling points. In Test 2, $\mathrm{wid}(\widetilde{\mathcal{I}}_t) < \varpi$ is satisfied in advance of $\mathrm{wid}(\widetilde{\mathcal{I}}_t + \widetilde{\mathcal{I}}_{\delta,t}) < \pi - 2R$. In Test 3, since $\varpi = \infty$, the condition $\mathrm{wid}(\widetilde{\mathcal{I}}_t) < \varpi$ is abandoned. Hence, the computational burden is reduced to the greatest extent.

The results are shown in Fig. 7. It is observed that the true values of the robot's orientation are included in the upper and lower bounds. In Test 2 and Test 3, we observe that the bounds of the estimation interval are as sharp as sawtooth, which get sharper with a higher correction frequency using visual orientation measurement. It can also be observed that the midpoint of the estimation interval is as sharp as stairs, which is caused by the sensor-less orientation prediction. Because the robot's heading rate δ_t in (17a) is not measured by a sensor, the estimation could only be calculated by maintaining the midpoint and expanding the bounds. Additionally, as shown in the results from

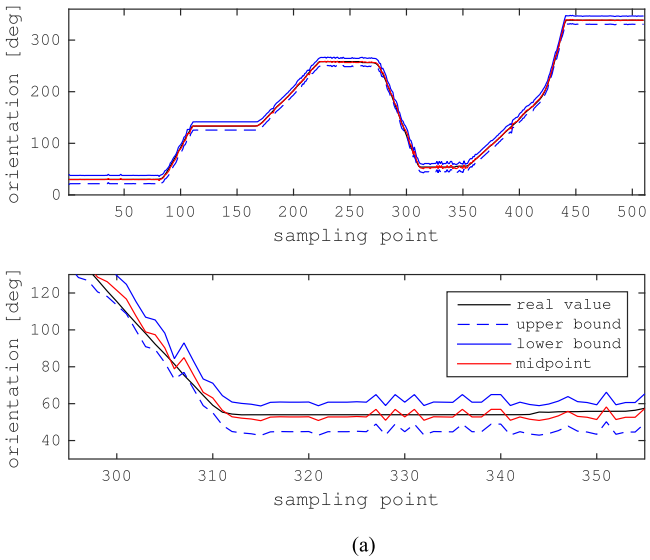

(a)

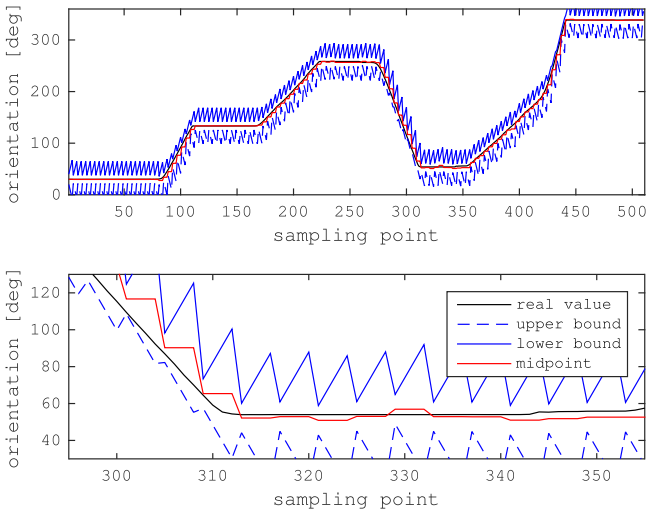

(b)

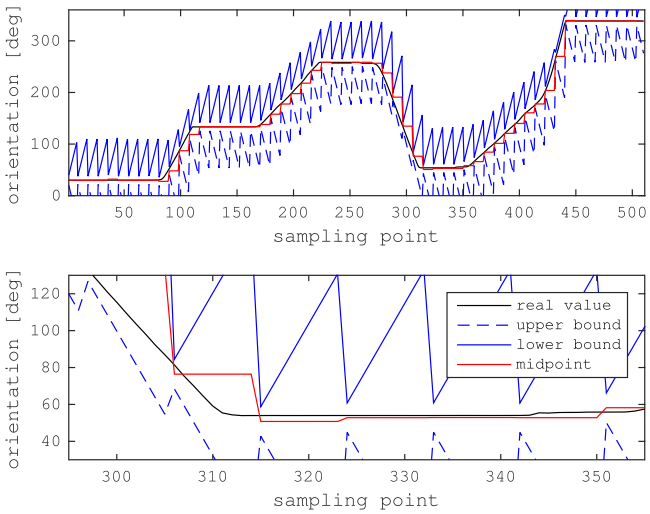

(c)

Fig. 7. Results of the orientation estimation of FVC. Partial regions of the upper figures are enlarged as shown in the lower ones. (a) Results of Test 1. (b) Results of Test 2. (c) Results of Test 3.

sampling point 300 to 310 in Test 2 and Test 3, the estimation midpoint is biased when the robot's orientation is changing. In fact, the interval arithmetics based estimation algorithm does not provide any optimal point estimation. In other words, all points in the estimation interval share the equal probability to be the true value of the robot's orientation.

Because FVC does not resort to any proprioceptive sensors (e.g., a gyroscope), the FVC in event-triggered mode has a large bias between two successive triggered point. Using a gyroscope to assist FVC, which is referred to as GyroFVC, could improve the performance of FVC to some extent. Denote ω_t as the gyroscopic reading at sampling point t. Considering the gyroscopic noise, which is assumed to be unknown-but-unbounded, we denote Δ as the error radius. Thus, after rewriting (17b) as $\delta_t \in \mathcal{I}_{\delta,t} = \mathcal{I}(\omega_t, \Delta)$, the same orientation estimation algorithm can be used to GyroFVC directly. Three tests are conducted similarly to the FVC, and their results are shown in Fig. 8. Observe the performance during the period between two successive visual orientation measurement-based (VOM-based) correction. The orientation estimation error of the GyroFVC increases slowly, because of the accumulation of gyroscopic error. It can be also observed that the frequency of VOM-based correction of GyroFVC is much lower than that of FVC, since $\Delta \ll \mathrm{rad}(\mathcal{W})$.

Define the root mean squared error (RMSE) as

$$\mathrm{RMSE} = \sqrt{\frac{\sum_{t=1}^{N} \left(\hat{\theta}_t - \theta_t\right)^2}{N}} \tag{27}$$

where N denotes the sampling amounts. If we take the midpoint of the estimation interval as the point estimation, the RMSE of Test 1, 2, and 3 for FVC and GyroFVC are shown in Table II. Obviously, the GyroFVC has higher accuracy than FVC when they are not in the event-triggered mode. In Tests 2 and 3, the GyroFVC has lower accuracy than FVC. It does not mean that FVC is better, because GyroFVC is not corrected by VOM as frequently as FVC.

We define the correction interval by the amount of sampling points between two successive VOM-based corrections. The relationship between the RMSE of orientation estimation and the correction interval are shown in Fig. 9. Obviously, the RMSE increases with the correction interval increasing, both for FVC and GyroFVC. However, to achieve the same accuracy, the GyroFVC has larger correction interval, namely, lower correction frequency. For example, if the RMSE should be guaranteed around 4 deg, then the VOM-based correction should be done every 3 sampling points for FVC, and 34 sampling points for GyroFVC. Hence, the introduction of gyroscope can reduce the computational burden dramatically.

3) Comparison Experiment: Experimental comparisons between magnetic and nonmagnetic compasses are done to show the robustness of the FVC against magnetic interference and motion blur.

In Test 1, the robot traverses an area with abundant ferromagnetic materials, while logging the readings of the gyroscope, magnetometer, and camera. Due to the geomagnetic distortion, the magnetometer-based compass becomes unreliable. In [6], a

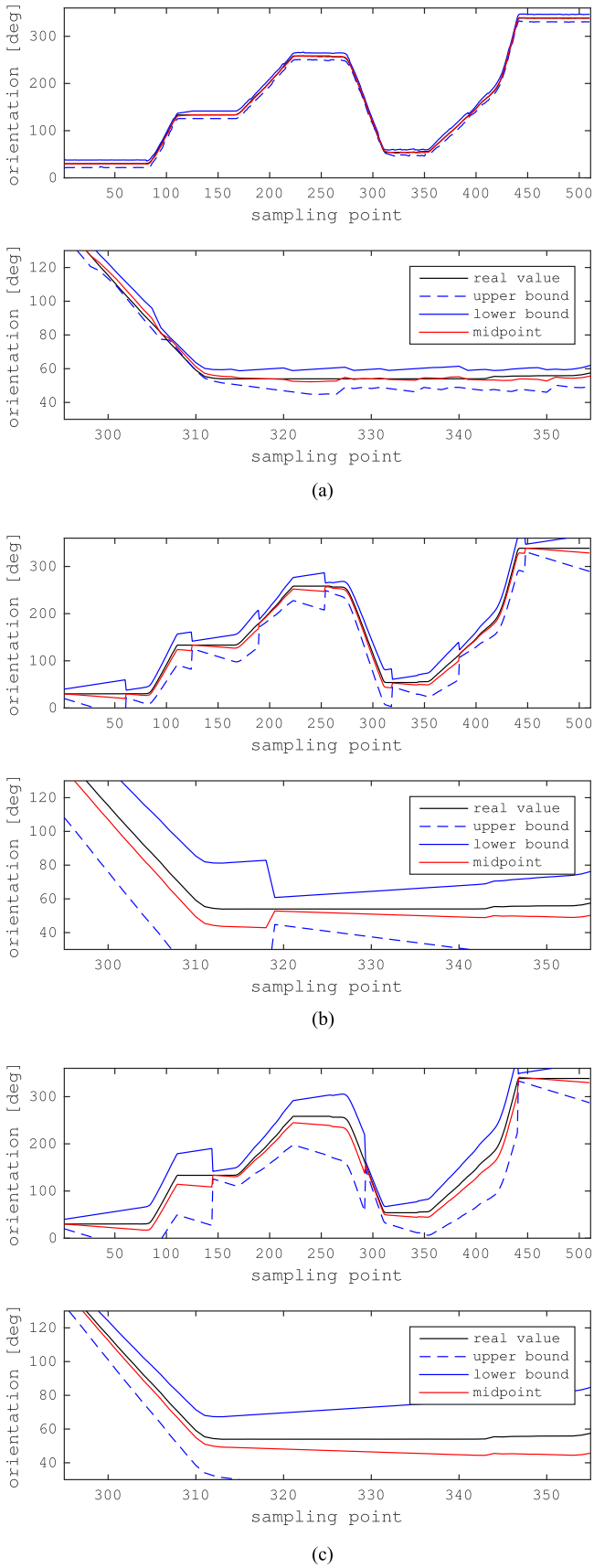

Fig. 8. Results of the orientation estimation of GyroFVC. Partial regions of the upper figures are enlarged as shown in the lower ones. (a) Results of Test 1. (b) Results of Test 2. (c) Results of Test 3.

TABLE II
RMSE OF TEST 1, 2, AND 3 FOR FVC AND GYROFVC

	Test 1	Test 2	Test 3
FVC	1.53 deg	4.95 deg	11.05 deg
GyroFVC	1.04 deg	6.01 deg	13.04 deg

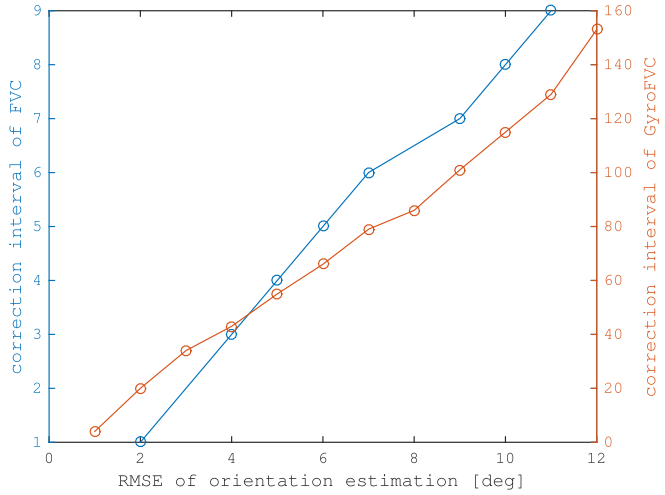

Fig. 9. Relationship between the RMSE of orientation estimation and the correction interval.

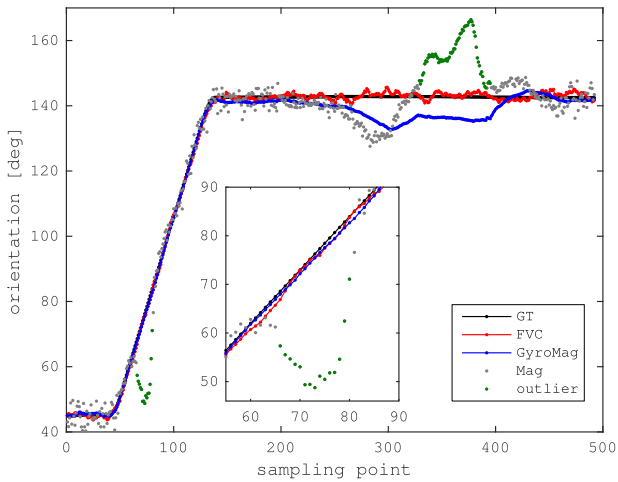

Fig. 10. Results of Test 1. "GT" stands for the ground truth, "Mag" stands for the magnetometer-based compass, "GyroMag" stands for the gyroscope-magnetometer integrated compass. The outliers of Mag recognized by GyroMag are marked in green.

gyroscope-magnetometer integrated compass is proposed. With the aid of a gyroscope, the measurements polluted by ferromagnetic interference are recognized and isolated; and finally, the robot's orientation estimation is estimated by using a self-tuning fault-tolerant Kalman filter. The experiment results of the FVC, the magnetometer-based compass, and gyroscope-magnetometer integrated compass proposed in [6] are shown in Fig. 10. It is observed that the magnetometer-based compass is unreliable during the period roughly from sampling point 65

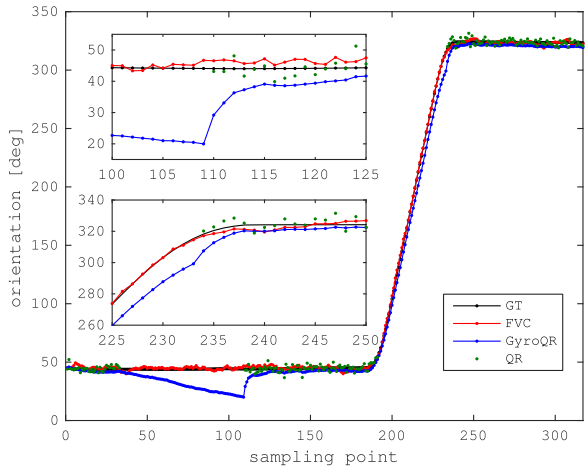

Fig. 11. Results of Test 2. "GT" stands for the ground truth, "GyroQR" stands for the gyroscope-QR integrated compass, and "QR" stands for the QR-based compass.

to 85, and 190 to 450, which may be caused by the ferromagnetic interference. In the absence of interference, the accuracy of FVC is almost equal to that of the gyroscope-magnetometer integrated compass, but higher than that of the magnetometer-based compass. In the presence of interference, only parts of the ferromagnetics-induced outliers are recognized correctly. The ferromagnetic interference renders a degradation in accuracy to the gyroscope-magnetometer integrated compass, if the outliers cannot be isolated. Because of the property that the Kalman filter tracks the measurements strongly, the outliers, which are not isolated, give rise to a large bias in orientation estimation. As a nonmagnetic compass, the FVC outperforms the magnetic compass in the presence of ferromagnetic interference.

In Test 2, the robot moves along a straight line at a speed up to 0.4 m/s, and rotates at a speed up to 40 deg/s, while logging the readings of the gyroscope and camera at 5 Hz. As a nonmagnetic compass, the QR-based compass is not sensitive to magnetic interference. However, due to the motion blur, the QR code laid on the floor may be unrecognizable; and therefore, the QR-based compass cannot be applied to a robot moving at a high speed. In [22], a gyroscope is utilized to alleviate this restriction. The fusion of gyroscope and QR-based compass can be described as a state estimation problem with intermittent measurements. With resorting to the gyroscope, the orientation is estimated only using gyroscopic readings at the sampling point when the QR code cannot be detected. The test results of FVC, the QR-based compass, and gyroscope-QR integrated compass proposed in [22] are shown in Fig. 11. It is observed that the there are no available measurements during the period from 35 to 110, and from 190 to 230, which is caused by the image blur. In contrast, the FVC maintains the orientation estimation with high accuracy throughout the test.

VI. Conclusion

In this paper, we proposed a novel nonmagnetic compass named FVC for mobile robots, which is suitable for the applications in indoor scenarios, especially the industrial environmental, which is full of ferro and electromagnetic interference. After the layout of the auxiliary strips parallel to the reference axis, the FVC was able to acquire the visual orientation measurement by analyzing the floor images. We designed an orientation estimation algorithm by means of interval arithmetics, coupled with an event trigger to reduce the algorithms computational complexity. In the end, we exhibited the procedure of the visual orientation measurement, the comparison experiments of the FVC, and two state-of-the-art compasses, which verifies the effectiveness of the proposed nonmagnetic compass.

There are some technical discussions on the proposed FVC. First, illumination is a factor that affects the FVC performance. To deal with this matter, the FVC is preferably used in a controlled environment where appropriate illumination can be guaranteed, otherwise each camera may be equipped with an embedded light to reduce the dependency of the FVC on the environmental illumination. It is also encouraged to paint the auxiliary strips with fluorescent materials to enable the FVC functioning for a short term in darkness. Second, severe camera shake can be detected by an accelerometer and vision itself may not be enough to deal with it. We will consider in the future work to extend FVC to be applicable in the uncontrolled outdoor environments with a stabilizer or antijitter algorithm. Third, to maintain robustness against interference objects, algorithms capable of distinguishing the auxiliary strips from nonauxiliary-strip objects are to be developed.

It is also interesting to notice that the mechanism of our proposed compass has its biological resembles. For example, avian creatures have the capability of finding the angles between its heading direction and a reference line by classical sensing effect [23] or quantum sensing effects [24], [25]. By examining such mechanisms in depth may be of great reference value in our future work.

References

[1] J. Simanek, M. Reinstein, and V. Kubelka, "Evaluation of the EKF-based estimation architectures for data fusion in mobile robots," *IEEE/ASME Trans. Mechatronics*, vol. 20, no. 2, pp. 985–990, Apr. 2015.

[2] S.-B. Kim, J.-C. Bazin, H.-K. Lee, K.-H. Choi, and S.-Y. Park, "Ground vehicle navigation in harsh urban conditions by integrating inertial navigation system, global positioning system, odometer and vision data," *IET Radar, Sonar Navig.*, vol. 5, no. 8, pp. 814–823, 2011.

[3] D. González, J. Pérez, V. Milanés, and F. Nashashibi, "A review of motion planning techniques for automated vehicles," *IEEE Trans. Intell. Transp. Syst.*, vol. 17, no. 4, pp. 1135–1145, Apr. 2016.

[4] M. Reinstein, V. Kubelka, and K. Zimmermann, "Terrain adaptive odometry for mobile skid-steer robots," in *Proc. IEEE Int. Conf. Robot. Autom.*, 2013, pp. 4706–4711.

[5] H.-Y. Chung, C.-C. Hou, and Y.-S. Chen, "Indoor intelligent mobile robot localization using fuzzy compensation and Kalman filter to fuse the data of gyroscope and magnetometer," *IEEE Trans. Ind. Electron.*, vol. 62, no. 10, pp. 6436–6447, Oct. 2015.

[6] W. Lv, Y. Kang, and J. Qin, "Indoor localization for skid-steering mobile robot by fusing encoder, gyroscope, and magnetometer," *IEEE Trans. Syst., Man, Cybern., Syst.*, to be published, doi: 10.1109/TSMC.2017.2701353.

[7] R. Siegwart, I. R. Nourbakhsh, and D. Scaramuzza, *Introduction to Autonomous Mobile Robots*, 2nd ed. Cambridge, MA, USA: MIT Press, 2011.

[8] C.-H. Tu, K. Tu, F.-R. Chang, and L.-S. Wang, "GPS compass: novel navigation equipment," *IEEE Trans. Aerosp. Electron. Syst.*, vol. 33, no. 3, pp. 1063–1068, Jul. 1997.

[9] J.-C. Juang and C.-F. Lin, "A sensor fusion scheme for the estimation of vehicular speed and heading angle," *IEEE Trans. Veh. Technol.*, vol. 64, no. 7, pp. 2773–2782, Jul. 2015.
[10] Z. Chen, H. Zou, H. Jiang, Q. Zhu, Y. C. Soh, and L. Xie, "Fusion of wifi, smartphone sensors and landmarks using the kalman filter for indoor localization," *Sensors*, vol. 15, no. 1, pp. 715–732, 2015.
[11] J. P. How, B. Behihke, A. Frank, D. Dale, and J. Vian, "Real-time indoor autonomous vehicle test environment," *IEEE Control Syst. Mag.*, vol. 28, no. 2, pp. 51–64, 2008.
[12] S. Hoermann and P. V. K. Borges, "Vehicle localization and classification using off-board vision and 3-d models," *IEEE Trans. Robot.*, vol. 30, no. 2, pp. 432–447, Apr. 2014.
[13] L. B. Marinho, J. S. Almeida, J. W. M. Souza, V. H. C. Albuquerque, and P. P. Rebouças Filho, "A novel mobile robot localization approach based on topological maps using classification with reject option in omnidirectional images," *Expert Syst. Appl.*, vol. 72, pp. 1–17, 2017.
[14] L. Cong, E. Li, H. Qin, K. V. Ling, and R. Xue, "A performance improvement method for low-cost land vehicle GPS/MEMS-INS attitude determination," *Sensors*, vol. 15, no. 3, pp. 5722–5746, 2015.
[15] W. Winterhalter, F. Fleckenstein, B. Steder, L. Spinello, and W. Burgard, "Accurate indoor localization for RGB-D smartphones and tablets given 2D floor plans," in *Proc. IEEE Int. Conf. Robot. Autom.*, 2015, pp. 3138–3143.
[16] C. Forster, Z. Zhang, M. Gassner, M. Werlberger, and D. Scaramuzza, "SVO: Semidirect visual odometry for monocular and multicamera systems," *IEEE Trans. Robot.*, vol. 33, no. 2, pp. 249–265, Apr. 2017.
[17] V. Usenko, J. Engel, J. Stückler, and D. Cremers, "Direct visual-inertial odometry with stereo cameras," in *Proc. IEEE Int. Conf. Robot. Autom.*, 2016, pp. 1885–1892.
[18] D. Xu, L. Han, M. Tan, and Y. F. Li, "Ceiling-based visual positioning for an indoor mobile robot with monocular vision," *IEEE Trans. Ind. Electron.*, vol. 56, no. 5, pp. 1617–1628, May 2009.
[19] D. Chen, Z. Peng, and X. Ling, "A low-cost localization system based on artificial landmarks with two degree of freedom platform camera," in *Proc. IEEE Int. Conf. Robot. Biomimetics.*, 2014, pp. 625–630.
[20] R. E. Moore, R. B. Kearfott, and M. J. Cloud, *Introduction to Interval Analysis*. Philadelphia, PA, USA: SIAM Press, 2009.
[21] J. K. Bekkeng, "Calibration of a novel MEMS inertial reference unit," *IEEE Trans. Instrum. Meas.*, vol. 58, no. 6, pp. 1967–1974, Jun. 2009.
[22] P. Nazemzadeh, D. Fontanelli, D. Macii, and L. Palopoli, "Indoor localization of mobile robots through QR code detection and dead reckoning data fusion," *IEEE/ASME Trans. Mechatronics*, vol. 22, no. 6, pp. 2588–2599, Dec. 2017.
[23] X. Long, J. Ye, D. Zhao, and S.-J. Zhang, "Magnetogenetics: remote non-invasive magnetic activation of neuronal activity with a magnetoreceptor," *Sci. Bull.*, vol. 60, no. 24, pp. 2107–2119, 2015.
[24] J. Pearson, G. Feng, C. Zheng, and G. Long, "Experimental quantum simulation of avian compass in a nuclear magnetic resonance system," *Sci. China Phys., Mechanics Astronomy*, vol. 59, no. 12, 2016, Art. no. 120312.
[25] J. Cai, G. G. Guerreschi, and H. J. Briegel, "Quantum control and entanglement in a chemical compass," *Phys. Rev. Lett.*, vol. 104, no. 22, 2010, Art. no. 220502.

Wenjun Lv received the Ph.D. degree in control science and engineering from the University of Science and Technology of China (USTC), Hefei, China, in 2018.

He is currently a Postdoctoral Fellow with the School of Information Science and Technology, USTC. His current research interests include state estimation, machine learning, and their application in robotics.

Yu Kang (M'09–SM'14) received the Ph.D. degree in control theory and control engineering from the University of Science and Technology of China (USTC), Hefei, China, in 2005.

From 2005 to 2007, he was a Postdoctoral Fellow with the Academy of Mathematics and Systems Science, Chinese Academy of Sciences, Beijing, China. He is currently a Professor with the State Key Laboratory of Fire Science, Department of Automation, and Institute of Advanced Technology, USTC, and with the Key Laboratory of Technology in GeoSpatial Information Processing and Application System, Chinese Academy of Sciences. His current research interests include monitoring of vehicle emissions, adaptive/robust control, variable structure control, mobile manipulator, and Markovian jump systems.

Yun-Bo Zhao (SM'14) received the B.Sc. degree in mathematics from the Shandong University, Jinan, China, in 2003, the M.Sc. degree in systems sciences from the Key Laboratory of Systems and Control, Chinese Academy of Sciences, Beijing, China, in 2007, and the Ph.D. degree in control engineering from the University of South Wales (formerly University of Glamorgan), Pontypridd, U.K., in 2008.

He has held postdoctoral positions with INRIA Grenoble, Grenoble, France, University of Glasgow, Glasgow, U.K., and Imperial College London, London, U.K., respectively. He is currently a Professor with the Zhejiang University of Technology, Hangzhou, China. His research interests include networked control systems, systems biology, and artificial intelligence.